

# Weak Distance Dependence of Hot-Electron-Transfer Rates at the Interface between Monolayer MoS<sub>2</sub> and Gold

Ce Xu, Hui Wen Yong, Jinlu He, Run Long, Alisson R. Cadore, Ioannis Paradisanos, Anna K. Ott, Giancarlo Soavi, Sefaattin Tongay, Giulio Cerullo, Andrea C. Ferrari,\* Oleg V. Prezhdo,\* and Zhi-Heng Loh\*



Cite This: ACS Nano 2021, 15, 819–828



Read Online

ACCESS |

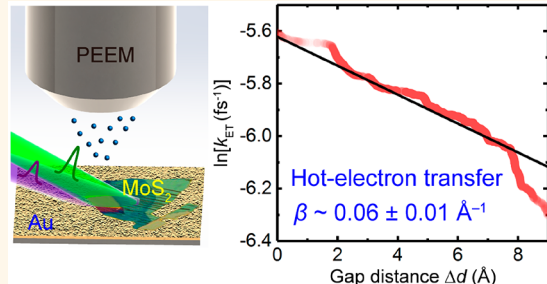
Metrics & More

Article Recommendations

Supporting Information

**ABSTRACT:** Electron transport across the transition-metal dichalcogenide (TMD)/metal interface plays an important role in determining the performance of TMD-based optoelectronic devices. However, the robustness of this process against structural heterogeneities remains unexplored, to the best of our knowledge. Here, we employ a combination of time-resolved photoemission electron microscopy (TR-PEEM) and atomic force microscopy to investigate the spatially resolved hot-electron-transfer dynamics at the monolayer (1L) MoS<sub>2</sub>/Au interface. A spatially heterogeneous distribution of 1L-MoS<sub>2</sub>/Au gap distances, along with the sub-80 nm spatial- and sub-60 fs temporal resolution of TR-PEEM, permits the simultaneous measurement of electron-transfer rates across a range of 1L-MoS<sub>2</sub>/Au distances. These decay exponentially as a function of distance, with an attenuation coefficient  $\beta \sim 0.06 \pm 0.01 \text{ \AA}^{-1}$ , comparable to molecular wires. *Ab initio* simulations suggest that surface plasmon-like states mediate hot-electron-transfer, hence accounting for its weak distance dependence. The weak distance dependence of the interfacial hot-electron-transfer rate indicates that this process is insensitive to distance fluctuations at the TMD/metal interface, thus motivating further exploration of optoelectronic devices based on hot carriers.

**KEYWORDS:** transition-metal dichalcogenides, TMD/metal interface, hot carriers, time-resolved photoemission electron microscopy, ultrafast spectroscopy



Transition-metal dichalcogenide monolayers (1L-TMDs) have electronic and optoelectronic properties<sup>1–4</sup> of technological significance, such as direct band gaps,<sup>5,6</sup> large exciton binding energies (0.24–0.96 eV),<sup>7–9</sup> high carrier mobilities ( $\sim 10^1\text{--}10^3 \text{ cm}^2\text{.V}\text{.s}^{-1}$ ),<sup>10–12</sup> superconductivity,<sup>13,14</sup> large nonlinear optical susceptibilities [ $\chi^{(2)} \sim 10^{-12} \text{ m.V}^{-1}$ ,  $\chi^{(3)} \sim 10^{-17}\text{--}10^{-19} \text{ m}^2\text{.V}^{-2}$ ],<sup>15</sup> and the addressability of the energetically degenerate K or K' valleys by valley-selective photoexcitation.<sup>16,17</sup> As a result of these properties, along with the ability to fabricate TMDs on wafer-scale,<sup>3,18–20</sup> these have found applications in photodetectors,<sup>21–23</sup> photovoltaics,<sup>24</sup> phototransistors,<sup>25,26</sup> and light-emitting diodes.<sup>27–29</sup>

In TMD-based devices, the TMD layer contacts a metal structure that is part of the electrical circuitry.<sup>30</sup> Electron transport at the TMD/metal interface therefore plays a crucial role in determining the final performance.<sup>31</sup> While much work has been done to explore means of minimizing the contact resistance at TMD/metal interfaces,<sup>32–35</sup> less known is how

interfacial structural heterogeneities influences electron transport efficiency. For example, in TMD-based thin-film transistors, irregularities at the TMD/metal interface result in a distribution of voltages across it, leading to contact noise.<sup>36–40</sup>

Studies of carrier dynamics provide insight into the electronic transport properties of materials.<sup>41,42</sup> While phenomena such as electron–electron<sup>43</sup> and electron–phonon scattering,<sup>43</sup> bandgap renormalization,<sup>44</sup> exciton formation,<sup>45</sup> diffusion,<sup>46</sup> and annihilation,<sup>47</sup> and carrier recombination<sup>48</sup> in TMDs have been investigated by ultrafast spectroscopy,<sup>49</sup> the dynamics of electron transport across TMD/metal interfaces is

Received: September 1, 2020

Accepted: December 8, 2020

Published: December 21, 2020



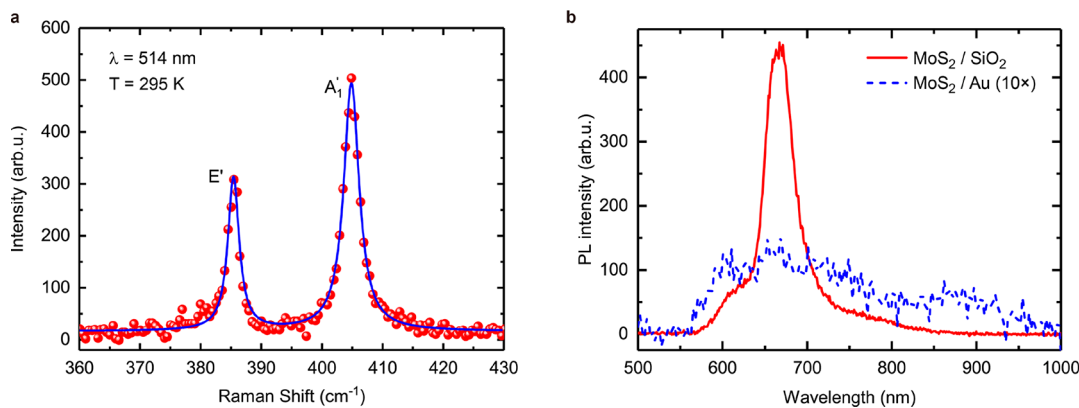


**Figure 1.** Spectroscopy of 1L- $\text{MoS}_2$  on Au. (a) Raman spectrum and fit to the sum of two Lorentzians. (b) PL spectra of 1L- $\text{MoS}_2/\text{SiO}_2$  and 1L- $\text{MoS}_2/\text{Au}$  collected under identical conditions.

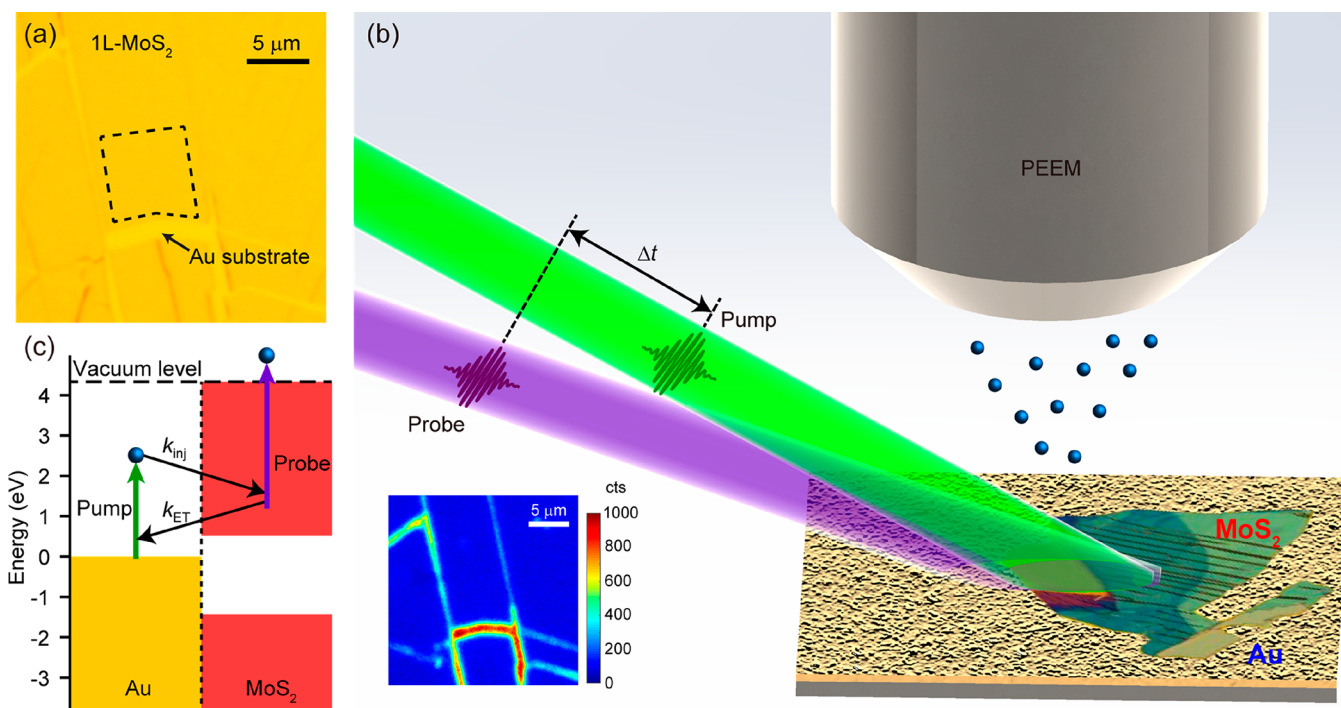


**Figure 2.** TR-PEEM probing of ultrafast electron transfer at the 1L- $\text{MoS}_2/\text{Au}$  interface. (a) Optical image of 1L- $\text{MoS}_2/\text{Au}$ , showing the outline of the region of interest. Broken regions allow access to the Au substrate (brighter areas). (b) 2.41 eV photoexcitation of 1L- $\text{MoS}_2/\text{Au}$  followed by 3.61 eV probe ejects photoelectrons from 1L- $\text{MoS}_2$ , collected and imaged by PEEM as a function of pump–probe time delay. (c) Band alignment of 1L- $\text{MoS}_2/\text{Au}$ , indicating the process of injection of electrons from Au into the 1L- $\text{MoS}_2$  conduction band, followed by electron transfer from 1L- $\text{MoS}_2$  to Au. TR-PEEM probes the population of conduction-band electrons in 1L- $\text{MoS}_2$  as a function of pump–probe time delay, giving  $k_{\text{ET}}$ .

still unexplored, to the best of our knowledge. Most time-resolved studies of TMDs are based on spatially averaged measurements, which do not address the effect on the carrier dynamics of spatial heterogeneity induced by defects. Time-resolved photoemission electron microscopy (TR-PEEM), which combines temporal and spatial resolution, was extended from studies of plasmon-polariton dynamics of metallic nanostructures<sup>50</sup> to visualize the spatially heterogeneous carrier dynamics of semiconductors,<sup>51–53</sup> including TMDs.<sup>54</sup> Its spatial resolution, up to  $\sim 4 \text{ nm}$ ,<sup>55</sup> makes it well-suited for investigating spatially resolved electronic transport at the TMD/metal interface.

Here, we employ TR-PEEM to investigate hot-electron transfer at the 1L- $\text{MoS}_2/\text{Au}$  interface. Electrons injected into

the 1L- $\text{MoS}_2$  conduction band undergo ultrafast transfer to the Au substrate on a  $\sim 0.4 \text{ ps}$  time scale. The lifetime map reveals spatially heterogeneous hot-electron-transfer rates, which correlate to the spatial distribution of 1L- $\text{MoS}_2/\text{Au}$  distances, as revealed by atomic force microscopy (AFM). The exponential distance dependence of the electron-transfer rate is characterized by an attenuation coefficient  $\beta \sim 0.06 \pm 0.01 \text{ \AA}^{-1}$ , comparable to molecular wires.<sup>56</sup> *Ab initio* simulations shed light on the origin of this small  $\beta$  value. The weak distance dependence suggests that interfacial hot-electron transfer is insensitive to distance fluctuations at TMD/metal interfaces, hence providing impetus for the exploration of optoelectronic devices that harness hot carriers.

## RESULTS AND DISCUSSION

Figure 1a is a representative Raman spectrum of a 1L-MoS<sub>2</sub> flake used for our experiments. The positions of the two main peaks are  $\sim 385.4\text{ cm}^{-1}$  for the in-plane  $E'$  mode, and  $\sim 404.9\text{ cm}^{-1}$  for the  $A_1'$  out-of-plane mode.<sup>57,58</sup> The difference between these modes is  $\sim 19.4\text{ cm}^{-1}$ , consistent with 1L-MoS<sub>2</sub>.<sup>57,58</sup> Photoluminescence (PL) spectra of 1L-MoS<sub>2</sub>/Au and 1L-MoS<sub>2</sub>/SiO<sub>2</sub> under identical conditions are in Figure 1b. The red curve is the PL spectrum of 1L-MoS<sub>2</sub>/SiO<sub>2</sub>. We assign the high-energy emission ( $\sim 616\text{ nm}$ ,  $\sim 2.01\text{ eV}$ ) to the recombination of B-excitons<sup>5</sup> and the lower energy one ( $\sim 664\text{ nm}$ ,  $\sim 1.87\text{ eV}$ ) to A-excitons.<sup>5</sup> The second-derivative spectrum shows the existence of a feature, red-shifted  $\sim 42\text{ meV}$  from the A-exciton transition (see Figure S2 of the Supporting Information). This red-shift is consistent with the range of binding energies for the A<sup>-</sup> trion;<sup>59</sup> therefore, we assign it to the A<sup>-</sup> trion PL. The blue curve is the 10 $\times$ -magnified PL spectrum of 1L-MoS<sub>2</sub>/Au, quenched by a factor  $\sim 19 \pm 3$  relative to the PL of 1L-MoS<sub>2</sub>/SiO<sub>2</sub>, possibly indicating electron transfer from MoS<sub>2</sub> to Au, suppressing radiative recombination.<sup>60–62</sup> The PL yield and lifetime of TMDs can also be influenced by the substrate in other ways, such as its doping concentration,<sup>63–66</sup> interfacial electron–phonon coupling,<sup>67</sup> dielectric tuning of exciton–exciton annihilation,<sup>68,69</sup> and field enhancement by the dielectric environment.<sup>65</sup> Plasmon-enhanced PL is not relevant in our work, given that quenching of PL is instead observed. Strong coupling between 1L-MoS<sub>2</sub> and Au could potentially occur, although its observation typically requires the embedding of the TMD in a microcavity or in a plasmonic structure.<sup>70</sup> Here, 1L-MoS<sub>2</sub> is placed on an Au-coated substrate, making strong light–matter coupling unlikely. A hallmark of strong coupling is the splitting of the exciton transition energy, observable in both the dark-field scattering and PL spectra.<sup>71</sup> Such a peak splitting is not observed in the PL spectra of Figure 1b, thus further ruling out strong light–matter coupling.

Photoexcitation of 1L-MoS<sub>2</sub>/Au (Figure 2a) at 2.41 eV results in the injection of electrons into the conduction band of 1L-MoS<sub>2</sub> (Figure 2b). These are subsequently ejected by a 3.61 eV UV probe pulse and refocused by a column of electron optics onto a 2D array detector, giving rise to the PEEM signal (Figure 2b). Based on the lateral momentum conservation requirements in photoemission<sup>72</sup> and the use of 3.61 eV probe pulses, we infer that direct injection of electrons in the conduction band of MoS<sub>2</sub> does not yield electrons in the probe window of the PEEM instrument (see Supporting Information for further details). On the other hand, photoexcitation of electrons near the Au Fermi level,  $E_F$ , creates hot electrons,<sup>73</sup> which then undergo ultrafast injection into the high-energy conduction-band states of 1L-MoS<sub>2</sub>, from which they can be photoemitted in the instrument probe window (Figure 2c).

TR-PEEM images for various pump–probe time delays are shown in Figure 3a. The temporal evolution of the TR-PEEM signal, spatially integrated over a 1L-MoS<sub>2</sub> region of interest, is reported in Figure 3b. The signal exhibits a prompt ( $\sim 50\text{ fs}$ , setup limited) response at time-zero, coincident with the peak of the signal from the Au substrate, followed by a delayed rise, to give a secondary peak that eventually decays on a sub-ps time scale. The signal prior to and at time-zero arises from the 3.61 eV pump and 2.41 eV probe in the pulse overlap region.<sup>54</sup> At a negative time delay, photoexcitation by the 3.61 eV pulse populates the 1L-MoS<sub>2</sub> conduction band near the  $\Gamma$  point. The

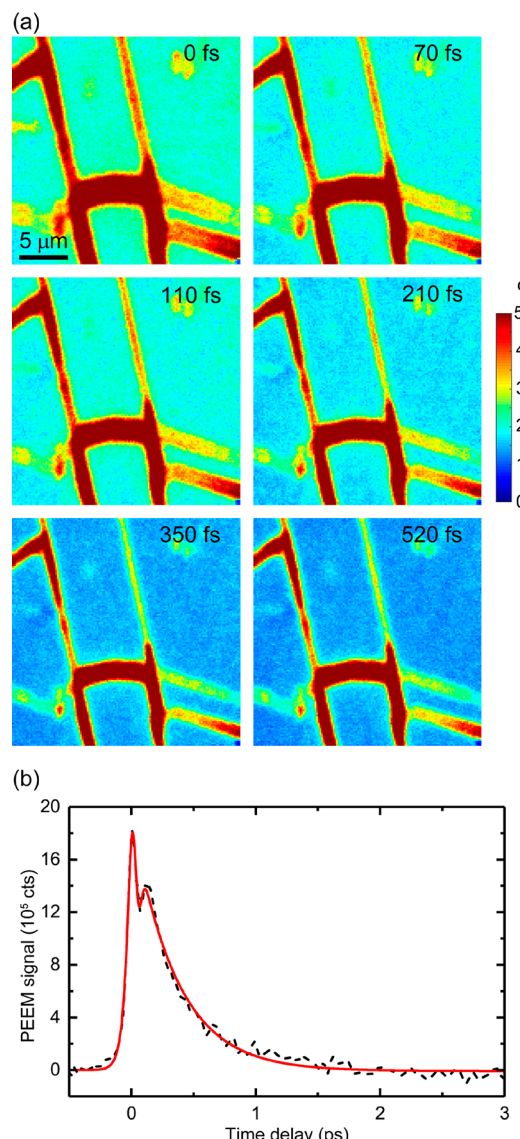


**Figure 3.** Time-resolved PEEM images as a function of time delay. (a) PEEM images collected in the vicinity of the region of interest shown in Figure 2a. Gaps in 1L-MoS<sub>2</sub> expose the Au substrate, giving rise to regions with a large number of counts. (b) Temporal evolution of the TR-PEEM signal, spatially integrated over the region of interest indicated in Figure 2a. The dashed line shows the data and the solid line the fit.

2.41 eV pulse then probes the relaxation of these high-energy electrons, hence giving rise to the dynamics observed at a negative time delay. The subsequent rise to give a secondary peak, delayed by  $\sim 0.12 \pm 0.01\text{ ps}$  relative to time-zero, reflects the injection of hot electrons from Au into the region of the 1L-MoS<sub>2</sub> conduction band in the probe window, consistent with previously observed sub-200 fs hot-electron transfer from Au nanoantennae to 1L-MoS<sub>2</sub>.<sup>74</sup> Intervalley scattering from the K valley, following 2.41 eV photoexcitation of 1L-MoS<sub>2</sub>, is ruled out as the origin of the rising signal because the lowest-energy band in the probe window, centered at  $\Gamma$ , lies  $\sim 0.7\text{ eV}$  above the conduction-band minimum at the K valley,<sup>7</sup> thus making such an energetically uphill intervalley scattering at room temperature unlikely. The TR-PEEM signal subsequently decays with  $\tau_{\text{ET}} \sim 351 \pm 6\text{ fs}$  as electrons leave the probe window.  $\tau_{\text{ET}}$  is independent of carrier density (see Supporting

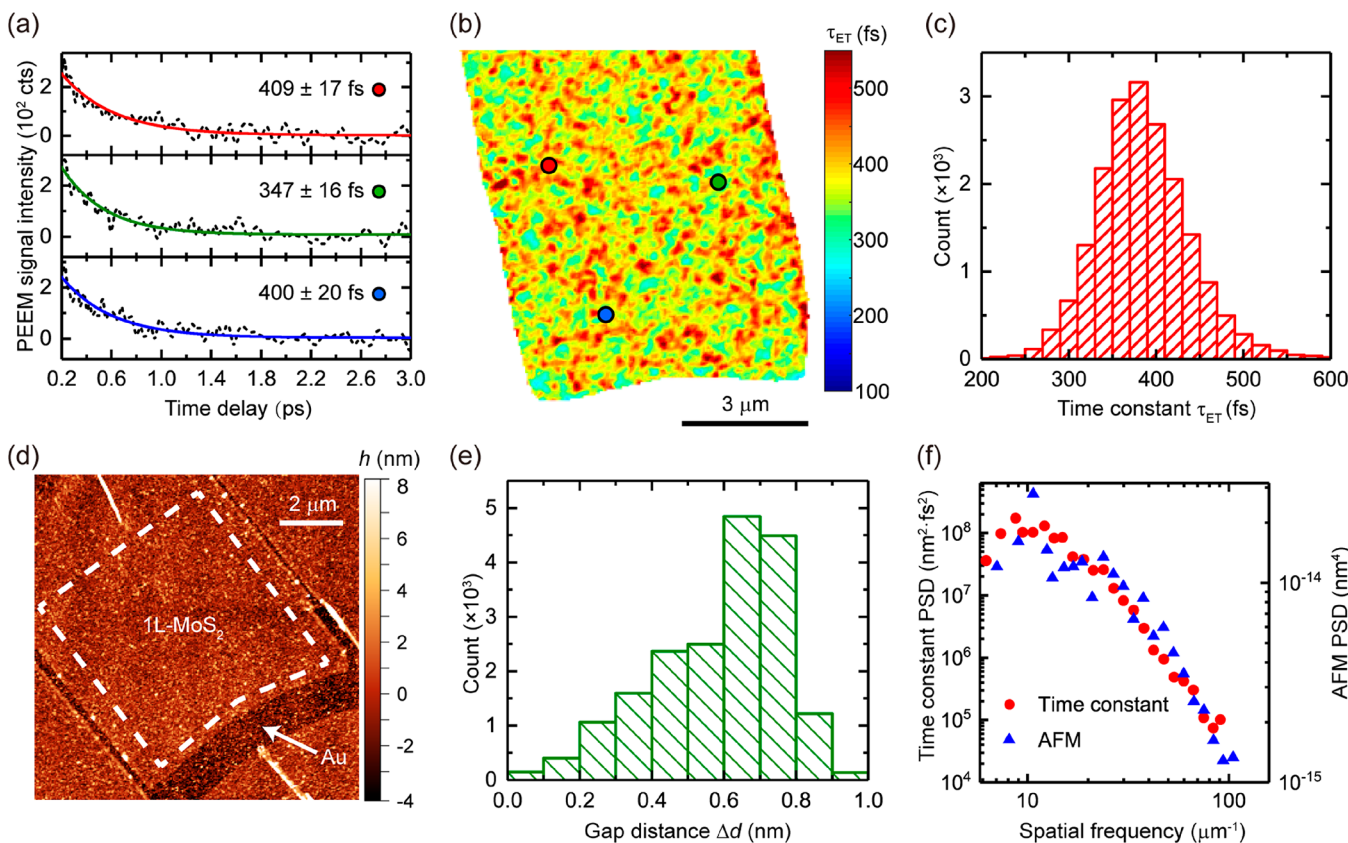


**Figure 4. Correlation of spatially heterogeneous interfacial  $\tau_{\text{ET}}$  and 1L-MoS<sub>2</sub>/Au gap distribution.** (a) Representative single-pixel time traces for different locations on the 1L-MoS<sub>2</sub> flake. The dashed lines are the data, and the solid lines are fits to a single exponential decay, with  $\tau_{\text{ET}}$  and corresponding standard errors of the fits given in the panel. (b)  $\tau_{\text{ET}}$  map, showing the spatial distribution and the locations from which the single-pixel traces in Figure 4a are extracted. (c)  $\tau_{\text{ET}}$  histogram. (d) AFM image of the region of interest. (e)  $\Delta d$  distribution. (f) FFT power spectral densities (PSDs) of  $\tau_{\text{ET}}$  map and AFM image, showing a similar dependence of FFT power on spatial frequency.

Information), ruling out carrier thermalization and carrier-LO-phonon scattering as its origin. Indeed, carrier thermalization speeds up with carrier density,<sup>41</sup> whereas carrier-LO-phonon scattering slows with carrier density, due to the hot-phonon effect.<sup>41</sup> Instead, based on the conduction-band minimum of 1L-MoS<sub>2</sub> being 0.52 eV above the Au  $E_F$ ,<sup>75</sup> we conclude that the sub-ps decay of the TR-PEEM signal arises from the back-electron transfer from the conduction band of 1L-MoS<sub>2</sub> to Au (Figure 2c). This assignment is supported by the ~19-fold reduction of the spectrally integrated PL of 1L-MoS<sub>2</sub> on Au as compared to SiO<sub>2</sub> (Figure 1b). Ultrafast electron transfer from the 1L-MoS<sub>2</sub> conduction band to Au facilitates nonradiative electron–hole recombination through the Au states before they enter the light cone, thus suppressing radiative recombination within 1L-MoS<sub>2</sub> and quenching its PL.<sup>60</sup> Indeed, optical pump–probe<sup>76</sup> and angle-resolved photo-emission<sup>75</sup> showed electron transfer from MoS<sub>2</sub> to Au on a sub-ps time scale.

To further investigate the dynamics of electron transfer from 1L-MoS<sub>2</sub> to Au, we extract the time traces for each individual pixel of the TR-PEEM image and fit them after a 0.2 ps time delay (after hot electron injection from Au to 1L-MoS<sub>2</sub> is completed) to a single exponential decay (Figure 4a).  $\tau_{\text{ET}}$  from each single-pixel time trace is used to construct a lifetime map (Figure 4b). This is analogous to that obtained from fluorescence lifetime imaging microscopy<sup>77</sup> and reveals the spatial distribution of  $\tau_{\text{ET}}$ . Figure 4c shows the corresponding  $\tau_{\text{ET}}$  histogram. This has a mean of ~386 fs and a standard

deviation of ~54 fs. The mean is in good agreement with the time constant obtained from fitting the spatially integrated time trace. The slight deviation is due to the fact that the lifetime obtained from the spatially integrated measurements represents an amplitude-weighted average time constant, instead of a simple average. The standard deviation, larger than the typical fitting error (~20 fs) for single-pixel time traces, suggests that the observed  $\tau_{\text{ET}}$  distribution primarily originates from spatial heterogeneity.

In order to elucidate the origin of the spatially heterogeneous  $\tau_{\text{ET}}$ , we use AFM to measure the heights of 1L-MoS<sub>2</sub> and Au substrate (Figure 4d). The Au substrate has a nm-scale roughness, which translates to roughness of the 1L-MoS<sub>2</sub> atop, hence a distribution of 1L-MoS<sub>2</sub>/Au gap distances  $\Delta d$  (Figure 4e). The  $\Delta d$  distribution is asymmetric due to the different widths and mean values of the  $h_{\text{MoS}_2}$  and  $h_{\text{Au}}$  height distributions (see Figure S6 of the Supporting Information). Ideally one would obtain a spatial map of  $\Delta d$  by separately measuring the heights of 1L-MoS<sub>2</sub> and the underlying Au substrate. In the absence of an experimental technique that can realize such a measurement, we employ an alternative procedure, assuming that an elevated 1L-MoS<sub>2</sub> region sits atop a higher part of the Au substrate, to extract the distribution of  $\Delta d$  (see the Supporting Information for details). Briefly, the heights of the 1L-MoS<sub>2</sub> and Au regions are separately sorted in ascending order. Taking the difference between each pair of 1L-MoS<sub>2</sub> and Au heights, and accounting for the offset introduced by the 1L-MoS<sub>2</sub> van der Waals

thickness of 0.676 nm, yields a distribution of  $\Delta d$ . Note that the region selected for our analysis is wrinkle-free, as shown in the AFM image of Figure 4d; the presence of wrinkles would weaken the correlation between the height of 1L-MoS<sub>2</sub> and the underlying Au substrate. Spatial fast Fourier transform (FFT) analysis reveals a similar dependence of the FFT power spectrum on the spatial frequency for both AFM image and  $\tau_{\text{ET}}$  map (Figure 4f). This suggests that the spatially heterogeneous  $\tau_{\text{ET}}$  map originates from surface roughness.

To gain further insight into the distance dependence of  $k_{\text{ET}} = 1/\tau_{\text{ET}}$ , we assume, based on the exponential decrease of through-space electronic coupling with distance,<sup>78</sup> that  $\tau_{\text{ET}}$  is inversely correlated with  $\Delta d$ . We thus plot  $\ln k_{\text{ET}}$  as a function of  $\Delta d$  in Figure 5; note that both  $k_{\text{ET}}$  and  $\Delta d$  values are

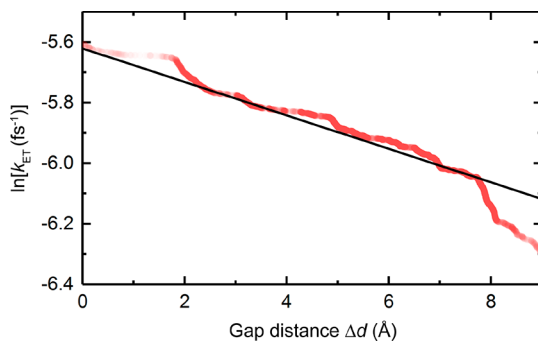


**Figure 5. Distance dependence of the hot-electron-transfer rate.** Dependence of  $k_{\text{ET}}$  on  $\Delta d$ , from a combination of  $\tau_{\text{ET}}$  and AFM maps. The dots are the data points, and the solid line is the fit to eq 1. The density of the data points reflects the density of  $\Delta d$  from AFM.

extracted from their respective histograms. This has  $\sim 20$ k data points and suggests a linear relation between  $\ln k_{\text{ET}}$  and  $\Delta d$ , *i.e.*, an exponential distance dependence of  $k_{\text{ET}}$ :

$$k_{\text{ET}} = k_0 \exp(-\beta \Delta d) \quad (1)$$

with pre-exponential factor  $k_0 \sim 5.79 \pm 0.53 \text{ ps}^{-1}$  and attenuation factor  $\beta \sim 0.06 \pm 0.01 \text{ Å}^{-1}$ . We note that typical  $\beta$  for saturated hydrocarbon bridges<sup>79</sup> is  $\sim 0.8\text{--}1 \text{ Å}^{-1}$ , whereas conjugated molecules, such as polyenes,<sup>80</sup> polyynes,<sup>81</sup> and phenylene<sup>82</sup> linkers, span  $\sim 0.1\text{--}0.6 \text{ Å}^{-1}$ . Conjugated molecular wires with small band gaps  $< 1 \text{ eV}$  can have  $\beta < 0.1 \text{ Å}^{-1}$ .<sup>55</sup> Our small  $\beta$ , comparable to those observed for molecular wires,<sup>56</sup> is unexpected when one considers the weak electronic coupling that exists at a van der Waals interface.<sup>83,84</sup> Electron transport within 1L-MoS<sub>2</sub>, such that interfacial electron transfer selectively occurs at a smaller range of  $\Delta d$ , could potentially account for the unusually small  $\beta$ . However, this is not a contributing factor for two reasons. First, based on the hot-electron diffusion coefficient of 1L-MoS<sub>2</sub> ( $\sim 18 \text{ cm}^2\cdot\text{s}^{-1}$ ),<sup>85</sup> we estimate that it would take a hot electron  $\sim 1.4 \text{ ps}$  to travel  $\sim 50 \text{ nm}$ , *i.e.*, the distance between adjacent pixels in the PEEM lifetime image. This time scale is substantially longer than, and therefore not competitive with, the observed  $\sim 0.35 \text{ ps}$  time constant for electron transfer at the 1L-MoS<sub>2</sub>/Au interface. Second, the intralayer transport of electrons within 1L-MoS<sub>2</sub>, from a region of larger  $\Delta d$  to one with smaller  $\Delta d$ , would give rise to an additional growth component at early ( $< 1 \text{ ps}$ ) time delays for time traces collected in regions of smaller  $\Delta d$ . Such a growth component is not observed in Figure 4a, thus further ruling out intralayer electron transport.

To shed light on the origin of the small  $\beta$ , we employ *ab initio* electronic structure calculations (see Methods for details) to investigate the nature of the 1L-MoS<sub>2</sub>/Au interaction. We consider high-energy conduction-band states of 1L-MoS<sub>2</sub>, accessed by photoexcitation and located in the probe window at the  $\Gamma$  point,  $\sim 1.6 \text{ eV}$  above  $E_F$ . Analysis of the partial density of states shows that such states split into two when the Au substrate is brought into the vicinity of 1L-MoS<sub>2</sub>. The energy splitting reflects the 1L-MoS<sub>2</sub>/Au coupling strength, hence  $k_{\text{ET}}$ . Increasing the distance between MoS<sub>2</sub> and Au results in an exponential decrease of  $V$ , with an attenuation factor  $\sim 0.21 \text{ Å}^{-1}$  (Figure 6a).

Plots of the electron density for such a high-energy conduction-band state reveal a significant delocalization from both 1L-MoS<sub>2</sub> and Au into the gap (Figure 6b). The most significant density peaks arising from Au are localized on the Au surface, outside the region occupied by the atoms. This contrasts the electron density plot for a lower-lying

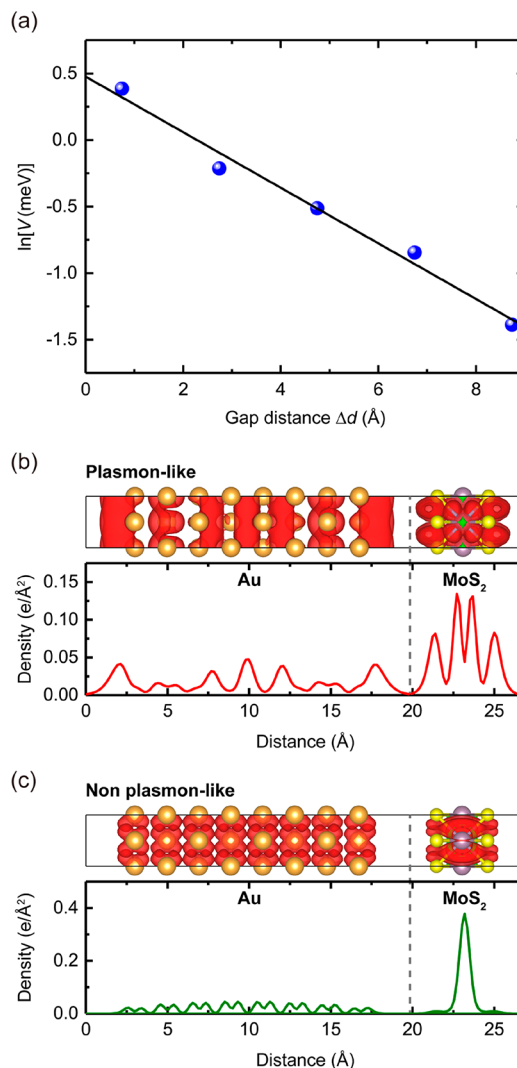


**Figure 6. *Ab initio* simulation of the 1L-MoS<sub>2</sub>/Au interaction.** (a) Calculated 1L-MoS<sub>2</sub>/Au interaction strength as a function of  $\Delta d$  (symbol) and fit to an exponential distance dependence. (b) Plasmon-like state and (c) nonplasmon-like state exhibit different delocalization of electrons into the 1L-MoS<sub>2</sub>/Au gap, as seen from the calculated electron densities (top panel) and their projections (bottom panel).  $\Delta d$  is 0.74 Å.

conduction-band state, which shows electrons bound tightly to the individual 1L-MoS<sub>2</sub> and Au layers (Figure 6c). The electron delocalization is reminiscent of the surface plasmon-like states, suggested in ref 86 to play a role in the electron-transfer dynamics of Au nanostructures interfaced to 1L-MoS<sub>2</sub>. The spatial delocalization of the Au electron density into the 1L-MoS<sub>2</sub>/Au gap supports the weak distance-dependent  $k_{ET}$  we observe. The calculated  $\beta \sim 0.21 \text{ \AA}^{-1}$  is larger than the experimental value because the 8-atom-thick Au slab in the simulations may not fully reproduce the spatial extent of the plasmon-like state in the experiment. We confirm this by repeating the simulations with a 10-atom-Au slab (see Figure S8 of the Supporting Information). These give  $\beta \sim 0.17 \text{ \AA}^{-1}$ , closer to the experimental value of  $\beta \sim 0.06 \text{ \AA}^{-1}$ . High-energy plasmon-like states ( $E - E_F > 1.6 \text{ eV}$ ) that may be accessed experimentally extend more into the 1L-MoS<sub>2</sub>/Au gap, especially for rough surfaces,<sup>87</sup> leading to an experimental  $\beta$  smaller than the computed one.

## CONCLUSIONS

We harnessed the spatial and temporal resolution of TR-PEEM, its large field-of-view, and the spatially heterogeneous distribution of 1L-MoS<sub>2</sub>/Au gap distances to determine the distance-dependent hot-electron-transfer dynamics across the 1L-MoS<sub>2</sub>/Au interface. Our approach seamlessly combines elements of electronic transport measurements performed at single-molecule junctions<sup>88,89</sup> with ultrafast spectroscopic probing of electron transfer in structurally well-defined donor-bridge-acceptor motifs,<sup>90</sup> both of which have elucidated distance- and molecular conformation-dependent electron-transfer rates. With improved temporal resolution, it may be possible to resolve the distance-dependent sub-100 fs electron injection rates at the 1L-MoS<sub>2</sub>/Au interface. In the present work, electron transfer likely occurs *via* incoherent hopping, considering that the probe window lies above the theoretically predicted tunneling barrier height<sup>91</sup> for the 1L-MoS<sub>2</sub>/Au interface and that  $\tau_{ET}$  exceeds the ~10 fs time scale for carrier dephasing<sup>43</sup> in 5L-MoS<sub>2</sub>. The small attenuation factor suggests that the transport of hot electrons across a 1L-MoS<sub>2</sub>/Au interface is robust against surface corrugations and defects. This finding, which contrasts with the interface sensitivity of transport of low-energy charge carriers in TMD-based electronic devices,<sup>36,37</sup> provides further impetus for realizing optoelectronic devices that harness hot carriers.<sup>92,93</sup>

## METHODS

**Sample Preparation.** The 1L-MoS<sub>2</sub>/Au interface is prepared as follows: 2H-MoS<sub>2</sub> flakes grown by chemical vapor transport<sup>94</sup> are exfoliated by micromechanical cleavage on Nitto Denko tape,<sup>95</sup> then exfoliated again on a polydimethylsiloxane (PDMS) stamp placed on a glass slide for inspection under an optical microscope.<sup>96</sup> Optical contrast, photoluminescence (PL) and Raman spectroscopies are used to identify 1L-MoS<sub>2</sub> prior to transfer. Raman and PL measurements<sup>58,97</sup> are performed at room temperature using a Horiba LabRam HR Evolution at 514 nm. PL measurements are performed with an incident power ~0.1 mW and a focal spot size of ~1 μm. 2 × 2 mm<sup>2</sup> prepatterned Au/Cr (50/2 nm) pads are defined by shadow mask, using Kapton tape on 90 nm SiO<sub>2</sub>/Si, followed by thermal evaporation at ~5 × 10<sup>-7</sup> Torr at 0.5 Å/s. Before transfer, the Au surface is cleaned in acetone and isopropanol for 30 s each, followed by 60 s of plasma treatment at 10 W. 1L-MoS<sub>2</sub> flakes are then aligned on the Au pads and stamped using xyz micro-manipulators.<sup>14,98</sup>

**Atomic Force Microscopy.** To characterize the separation distance between 1L-MoS<sub>2</sub> and Au after 1L-MoS<sub>2</sub> transfer, AFM is performed with a Bruker Dimension Icon system in peak-force tapping mode, with a topography resolution of ~50 pm. From our AFM measurements, the Si/SiO<sub>2</sub> substrate roughness is ~0.2–0.3 nm, while that of Au is ~1.6 nm. The resolution of the AFM is therefore sufficient to detect the roughness of the 1L-MoS<sub>2</sub> and the underlying Au substrate. It is well-known that the AFM height of 1L-layered materials (1L-LMs) on a substrate does usually reproduce the theoretical thickness.<sup>99</sup> This is related to different parameters: the roughness of the substrate, the force of interaction between 1L-LM and substrate, and the presence of trapped contaminants. For example, even for a single layer of graphene, measured AFM thicknesses of ~1.8 nm are common, depending on peak force and substrate.<sup>100</sup> Therefore, the height of 1L-MoS<sub>2</sub> on Au is also affected. The height of 1L-MoS<sub>2</sub> is predicted to be ~0.7 nm,<sup>101</sup> while the experimental thickness by AFM is expected to be higher, due to the factors discussed above. For example, ref 102 reported 1L-WSe<sub>2</sub> on Au with a thickness ~2.4 nm, attributed to water molecules trapped between 1L-WSe<sub>2</sub> and Au, while ref 101 reported ~1.6 nm for 1L-MoS<sub>2</sub> on hBN, assigned to PDMS residues trapped between both materials. Our AFM data indicate a 1L-MoS<sub>2</sub> height ~1.3 nm, lower than expected for PDMS contaminants.<sup>101</sup> We also remove contaminants from the interface by performing transfer according to ref 103. As such, we believe that the 1L-MoS<sub>2</sub> height of ~1.3 nm is related to the Au film roughness and the difference in the AFM tip interaction with 1L-MoS<sub>2</sub> and Au.

**Ultrafast Photoemission Electron Microscopy.** We use a high-repetition-rate, high-power Yb fiber laser (Tangerine 30, Amplitude Systemes), which delivers ~40 μJ, 320 fs pulses at 0.6 MHz and center wavelength (photon energy) of ~1.03 μm (1.20 eV). After spectral broadening in a Xe-filled hollow-core fiber,<sup>104</sup> a combination of highly dispersive chirped mirrors and a pair of wedges are employed to compress the laser pulses to 50 fs full-width-at-half-maximum (FWHM) duration. The second and third harmonics, with photon energies ~2.41 and 3.61 eV, respectively, are generated through a series of nonlinear frequency conversion steps in β-barium borate crystals, followed by temporal compression using a prism pair. The FWHM of the second harmonic, which acts as a pump beam, is ~46 fs, whereas the pulse duration of the third harmonic, acting as a probe, is ~40 fs. The pump beam is sent into a computer-controlled optical delay line to vary the time delay between pump and probe pulses. The overall time resolution, as determined by pump–probe cross-correlation at the sample position, is ~55 fs FWHM. The PEEM microscope (Focus GmbH, PEEM-IS) has a spatial resolution of ~77 nm according to the 16–84% criterion, defined as the distance over which the image intensity decreases from 84% to 16% of its maximum value.<sup>53,105</sup> At each time delay, the image acquisition time is 19s. We use an average of three independent data sets.

**Ab Initio Electronic Structure Calculations.** We use a periodically repeated slab with two materials: a 16-atom Au (001) surface and 6-atom 1L-MoS<sub>2</sub>. The supercell parameters are 5.46 and 3.15 Å in the *a* and *b* directions, respectively, with a 20 Å vacuum depth along the surface normal. To determine the distance-dependent electron-transfer rate, various Au–S separation distances of ~0.74, 2.74, 4.74, 6.74, and 8.74 Å between the two slabs are used. The electronic structure calculation is performed with the Vienna *ab initio* simulation package (VASP).<sup>106</sup> The exchange and correlation effects are described by the Perdew–Burke–Ernzerhof functional.<sup>107</sup> The interaction between ionic cores and valence electrons is treated by the projector-augmented wave (PAW) method.<sup>108</sup> The van der Waals interactions are described by the Grimme DFT-D3 approach.<sup>109</sup> An energy cutoff ~400 eV is used for the electronic structure calculations. A dense Monkhorst–Pack *k*-point mesh of 97 × 97 × 1 is used to obtain an accurate density of states.<sup>110</sup>

## ASSOCIATED CONTENT

## SI Supporting Information

The Supporting Information is available free of charge at <https://pubs.acs.org/doi/10.1021/acsnano.0c07350>.

Determination of spatial and temporal resolution, second derivative of the PL spectrum, determination of photon order and probe window, temporal response of the Au substrate, fluence dependence measurements, reconstruction of the  $\Delta d$  distribution, power spectral analysis of TR-PEEM and AFM data, and *ab initio* analysis of 1L-MoS<sub>2</sub>/Au interaction ([PDF](#))

## AUTHOR INFORMATION

## Corresponding Authors

**Andrea C. Ferrari** — Cambridge Graphene Centre, University of Cambridge, Cambridge CB3 0FA, United Kingdom; [orcid.org/0000-0003-0907-9993](https://orcid.org/0000-0003-0907-9993); Email: [acf26@eng.cam.ac.uk](mailto:acf26@eng.cam.ac.uk)

**Oleg V. Prezhdo** — Department of Chemistry, University of Southern California, Los Angeles, California 90089, United States; [orcid.org/0000-0002-5140-7500](https://orcid.org/0000-0002-5140-7500); Email: [prezhdo@usc.edu](mailto:prezhdo@usc.edu)

**Zhi-Heng Loh** — Division of Chemistry and Biological Chemistry, School of Physical and Mathematical Sciences and Centre for Optical Fibre Technology, The Photonics Institute, Nanyang Technological University, Singapore 637371, Singapore; [orcid.org/0000-0001-9729-9632](https://orcid.org/0000-0001-9729-9632); Email: [zhiheng@ntu.edu.sg](mailto:zhiheng@ntu.edu.sg)

## Authors

**Ce Xu** — Division of Chemistry and Biological Chemistry, School of Physical and Mathematical Sciences, Nanyang Technological University, Singapore 637371, Singapore

**Hui Wen Yong** — Division of Chemistry and Biological Chemistry, School of Physical and Mathematical Sciences, Nanyang Technological University, Singapore 637371, Singapore

**Jinlu He** — College of Chemistry, Key Laboratory of Theoretical and Computational Photochemistry, Beijing Normal University, Beijing 100875, People's Republic of China

**Run Long** — College of Chemistry, Key Laboratory of Theoretical and Computational Photochemistry, Beijing Normal University, Beijing 100875, People's Republic of China; [orcid.org/0000-0003-3912-8899](https://orcid.org/0000-0003-3912-8899)

**Alisson R. Cadore** — Cambridge Graphene Centre, University of Cambridge, Cambridge CB3 0FA, United Kingdom

**Ioannis Paradisanos** — Cambridge Graphene Centre, University of Cambridge, Cambridge CB3 0FA, United Kingdom

**Anna K. Ott** — Cambridge Graphene Centre, University of Cambridge, Cambridge CB3 0FA, United Kingdom

**Giancarlo Soavi** — Cambridge Graphene Centre, University of Cambridge, Cambridge CB3 0FA, United Kingdom; Institute for Solid State Physics, Abbe Center of Photonics, Friedrich-Schiller-University Jena, 07743 Jena, Germany; [orcid.org/0000-0003-2434-2251](https://orcid.org/0000-0003-2434-2251)

**Sefaattin Tongay** — School for Engineering of Matter, Transport, and Energy, Arizona State University, Tempe, Arizona 85287, United States; [orcid.org/0000-0001-8294-984X](https://orcid.org/0000-0001-8294-984X)

**Giulio Cerullo** — Department of Physics, Politecnico di Milano, I-20133 Milano, Italy; IFN-CNR, I-20133 Milano, Italy; [orcid.org/0000-0002-9534-2702](https://orcid.org/0000-0002-9534-2702)

Complete contact information is available at: <https://pubs.acs.org/10.1021/acsnano.0c07350>

## Notes

The authors declare no competing financial interest.

## ACKNOWLEDGMENTS

We acknowledge financial support from the A\*STAR Advanced Optics in Engineering Program (122 360 0008) and the Ministry of Education (MOE2018-T2-1-081 and RG109/18), the National Natural Science Foundation of China (grant no. 21973006), the EU Graphene and Quantum Flagships, ERC grants Hetero2D, GSYNCOR, EPSRC grants EP/L0160871/1, EP/K01711X/1, and EP/K017144/1, and the U.S. National Science Foundation (grant no. CHE-1900510).

## REFERENCES

- (1) Bonaccorso, F.; Sun, Z.; Hasan, T.; Ferrari, A. Graphene Photonics and Optoelectronics. *Nat. Photonics* **2010**, *4*, 611.
- (2) Wang, Q. H.; Kalantar-Zadeh, K.; Kis, A.; Coleman, J. N.; Strano, M. S. Electronics and Optoelectronics of Two-Dimensional Transition Metal Dichalcogenides. *Nat. Nanotechnol.* **2012**, *7*, 699.
- (3) Ferrari, A. C.; Bonaccorso, F.; Fal'Ko, V.; Novoselov, K. S.; Roche, S.; Bøggild, P.; Borini, S.; Koppens, F. H.; Palermo, V.; Pugno, N.; et al. Science and Technology Roadmap for Graphene, Related Two-Dimensional Crystals, and Hybrid Systems. *Nanoscale* **2015**, *7*, 4598–4810.
- (4) Liu, Y.; Weiss, N. O.; Duan, X.; Cheng, H.-C.; Huang, Y.; Duan, X. van der Waals Heterostructures and Devices. *Nat. Rev. Mater.* **2016**, *1*, 16042.
- (5) Splendiani, A.; Sun, L.; Zhang, Y.; Li, T.; Kim, J.; Chim, C.-Y.; Galli, G.; Wang, F. Emerging Photoluminescence in Monolayer MoS<sub>2</sub>. *Nano Lett.* **2010**, *10*, 1271–1275.
- (6) Mak, K. F.; Lee, C.; Hone, J.; Shan, J.; Heinz, T. F. Atomically Thin MoS<sub>2</sub>: A New Direct-Gap Semiconductor. *Phys. Rev. Lett.* **2010**, *105*, 136805.
- (7) Qiu, D. Y.; da Jornada, F. H.; Louie, S. G. Optical Spectrum of MoS<sub>2</sub>: Many-Body Effects and Diversity of Exciton States. *Phys. Rev. Lett.* **2013**, *111*, 216805.
- (8) Mostaani, E.; Szyniszewski, M.; Price, C.; Maezono, R.; Danovich, M.; Hunt, R.; Drummond, N.; Fal'Ko, V. Diffusion Quantum Monte Carlo Study of Excitonic Complexes in Two-Dimensional Transition-Metal Dichalcogenides. *Phys. Rev. B: Condens. Matter Mater. Phys.* **2017**, *96*, 075431.
- (9) Park, S.; Mutz, N.; Schultz, T.; Blumstengel, S.; Han, A.; Aljarb, A.; Li, L.-J.; List-Kratochvil, E. J.; Amsalem, P.; Koch, N. Direct Determination of Monolayer MoS<sub>2</sub> and WSe<sub>2</sub> Exciton Binding Energies on Insulating and Metallic Substrates. *2D Mater.* **2018**, *5*, 025003.
- (10) Radisavljevic, B.; Kis, A. Mobility Engineering and a Metal-Insulator Transition in Monolayer MoS<sub>2</sub>. *Nat. Mater.* **2013**, *12*, 815.
- (11) Schmidt, H.; Giustiniano, F.; Eda, G. Electronic Transport Properties of Transition Metal Dichalcogenide Field-Effect Devices: Surface and Interface Effects. *Chem. Soc. Rev.* **2015**, *44*, 7715–7736.
- (12) Liao, W.; Zhao, S.; Li, F.; Wang, C.; Ge, Y.; Wang, H.; Wang, S.; Zhang, H. Interface Engineering of Two-Dimensional Transition Metal Dichalcogenides towards Next-Generation Electronic Devices: Recent Advances and Challenges. *Nanoscale Horiz.* **2020**, *5*, 787–807.
- (13) Piatti, E.; De Fazio, D.; Daghero, D.; Tamalampudi, S. R.; Yoon, D.; Ferrari, A. C.; Gonnelli, R. S. Multi-Valley Superconductivity in Ion-Gated MoS<sub>2</sub> Layers. *Nano Lett.* **2018**, *18*, 4821–4830.

- (14) Orchin, G. J.; De Fazio, D.; Di Bernardo, A.; Hamer, M.; Yoon, D.; Cadore, A. R.; Goykhman, I.; Watanabe, K.; Taniguchi, T.; Robinson, J. W.; et al. Niobium Diselenide Superconducting Photodetectors. *Appl. Phys. Lett.* **2019**, *114*, 251103.
- (15) Säynätjoki, A.; Karvonen, L.; Rostami, H.; Autere, A.; Mehravar, S.; Lombardo, A.; Norwood, R. A.; Hasan, T.; Peyghambarian, N.; Lipsanen, H.; Kieu, K.; Ferrari, A. C.; Polini, M.; Sun, Z. Ultra-Strong Nonlinear Optical Processes and Trigonal Warping in MoS<sub>2</sub> Layers. *Nat. Commun.* **2017**, *8*, 893.
- (16) Mak, K. F.; He, K.; Shan, J.; Heinz, T. F. Control of Valley Polarization in Monolayer MoS<sub>2</sub> by Optical Helicity. *Nat. Nanotechnol.* **2012**, *7*, 494–498.
- (17) Wang, Z.; Molina-Sánchez, A.; Altmann, P.; Sangalli, D.; De Fazio, D.; Soavi, G.; Sassi, U.; Bottegoni, F.; Ciccacci, F.; Finazzi, M.; Wirtz, L.; Ferrari, A. C.; Marini, A.; Cerullo, G.; Dal Conte, S. Intravalley Spin-Flip Relaxation Dynamics in Single-Layer WS<sub>2</sub>. *Nano Lett.* **2018**, *18*, 6882–6891.
- (18) Bonaccorso, F.; Lombardo, A.; Hasan, T.; Sun, Z.; Colombo, L.; Ferrari, A. C. Production and Processing of Graphene and 2D Crystals. *Mater. Today* **2012**, *15*, 564–589.
- (19) Yu, H.; Liao, M.; Zhao, W.; Liu, G.; Zhou, X.; Wei, Z.; Xu, X.; Liu, K.; Hu, Z.; Deng, K.; et al. Wafer-Scale Growth and Transfer of Highly-Oriented Monolayer MoS<sub>2</sub> Continuous Films. *ACS Nano* **2017**, *11*, 12001–12007.
- (20) Backes, C.; Abdelkader, A. M.; Alonso, C.; Andrieux-Ledier, A.; Arenal, R.; Azpeitia, J.; Balakrishnan, N.; Banszerus, L.; Barjon, J.; Bartali, R. Production and Processing of Graphene and Related Materials. *2D Mater.* **2020**, *7*, 022001.
- (21) Koppens, F.; Mueller, T.; Avouris, P.; Ferrari, A.; Vitiello, M.; Polini, M. Photodetectors Based on Graphene, Other Two-Dimensional Materials and Hybrid Systems. *Nat. Nanotechnol.* **2014**, *9*, 780.
- (22) De Fazio, D.; Goykhman, I.; Yoon, D.; Bruna, M.; Eiden, A.; Milana, S.; Sassi, U.; Barbone, M.; Dumcenco, D.; Marinov, K.; et al. High Responsivity, Large-Area Graphene/MoS<sub>2</sub> Flexible Photodetectors. *ACS Nano* **2016**, *10*, 8252–8262.
- (23) Long, M.; Wang, P.; Fang, H.; Hu, W. Progress, Challenges, and Opportunities for 2D Material Based Photodetectors. *Adv. Funct. Mater.* **2019**, *29*, 1803807.
- (24) Das, S.; Pandey, D.; Thomas, J.; Roy, T. The Role of Graphene and Other 2D Materials in Solar Photovoltaics. *Adv. Mater.* **2019**, *31*, 1802722.
- (25) Huo, N.; Konstantatos, G. Ultrasensitive All-2D MoS<sub>2</sub> Phototransistors Enabled by an Out-Of-Plane MoS<sub>2</sub> PN Homojunction. *Nat. Commun.* **2017**, *8*, 572.
- (26) Gadelha, A. C.; Cadore, A. R.; Watanabe, K.; Taniguchi, T.; de Paula, A. M.; Malar, L. M.; Lacerda, R. G.; Campos, L. C. Gate-Tunable Non-Volatile Photomemory Effect in MoS<sub>2</sub> Transistors. *2D Mater.* **2019**, *6*, 025036.
- (27) Sundaram, R.; Engel, M.; Lombardo, A.; Krupke, R.; Ferrari, A.; Avouris, P.; Steiner, M. Electroluminescence in Single Layer MoS<sub>2</sub>. *Nano Lett.* **2013**, *13*, 1416–1421.
- (28) Withers, F.; Del Pozo-Zamudio, O.; Mishchenko, A.; Rooney, A.; Gholina, A.; Watanabe, K.; Taniguchi, T.; Haigh, S.; Geim, A.; Tartakovskii, A.; et al. Light-Emitting Diodes by Band-Structure Engineering in van der Waals Heterostructures. *Nat. Mater.* **2015**, *14*, 301.
- (29) Palacios-Berraquero, C.; Barbone, M.; Kara, D. M.; Chen, X.; Goykhman, I.; Yoon, D.; Ott, A. K.; Beitner, J.; Watanabe, K.; Taniguchi, T.; Ferrari, A. C.; Atatüre, M. Atomically Thin Quantum Light-Emitting Diodes. *Nat. Commun.* **2016**, *7*, 12978.
- (30) Radisavljevic, B.; Radenovic, A.; Brivio, J.; Giacometti, V.; Kis, A. Single-Layer MoS<sub>2</sub> Transistors. *Nat. Nanotechnol.* **2011**, *6*, 147.
- (31) Allain, A.; Kang, J.; Banerjee, K.; Kis, A. Electrical Contacts to Two-Dimensional Semiconductors. *Nat. Mater.* **2015**, *14*, 1195–1205.
- (32) Das, S.; Chen, H.-Y.; Penumatcha, A. V.; Appenzeller, J. High Performance Multilayer MoS<sub>2</sub> Transistors with Scandium Contacts. *Nano Lett.* **2013**, *13*, 100–105.
- (33) Kappera, R.; Voiry, D.; Yalcin, S. E.; Branch, B.; Gupta, G.; Mohite, A. D.; Chhowalla, M. Phase-Engineered Low-Resistance Contacts for Ultrathin MoS<sub>2</sub> Transistors. *Nat. Mater.* **2014**, *13*, 1128–1134.
- (34) Schulman, D. S.; Arnold, A. J.; Das, S. Contact Engineering for 2D Materials and Devices. *Chem. Soc. Rev.* **2018**, *47*, 3037–3058.
- (35) Wang, Y.; Kim, J. C.; Wu, R. J.; Martinez, J.; Song, X.; Yang, J.; Zhao, F.; Mkhyan, A.; Jeong, H. Y.; Chhowalla, M. van der Waals Contacts between Three-Dimensional Metals and Two-Dimensional Semiconductors. *Nature* **2019**, *568*, 70–74.
- (36) Renteria, J.; Samnakay, R.; Rumyantsev, S.; Jiang, C.; Goli, P.; Shur, M.; Balandin, A. Low-Frequency 1/f Noise in MoS<sub>2</sub> Transistors: Relative Contributions of the Channel and Contacts. *Appl. Phys. Lett.* **2014**, *104*, 153104.
- (37) Ghatak, S.; Mukherjee, S.; Jain, M.; Sarma, D.; Ghosh, A. Microscopic Origin of Low Frequency Noise in MoS<sub>2</sub> Field-Effect Transistors. *APL Mater.* **2014**, *2*, 092515.
- (38) Joo, M.-K.; Moon, B. H.; Ji, H.; Han, G. H.; Kim, H.; Lee, G.; Lim, S. C.; Suh, D.; Lee, Y. H. Understanding Coulomb Scattering Mechanism in Monolayer MoS<sub>2</sub> Channel in the Presence of h-BN Buffer Layer. *ACS Appl. Mater. Interfaces* **2017**, *9*, 5006–5013.
- (39) Kwon, J.; Prakash, A.; Das, S. R.; Janes, D. B. Correlating Electronic Transport and 1/f Noise in MoSe<sub>2</sub> Field-Effect Transistors. *Phys. Rev. Appl.* **2018**, *10*, 064029.
- (40) Kwon, J.; Park, J. H.; Delker, C. J.; Harris, C. T.; Swartzentruber, B.; Das, S. R.; Janes, D. B. Transitions between Channel and Contact Regimes of Low-Frequency Noise in Many-Layer MoS<sub>2</sub> Field Effect Transistors. *Appl. Phys. Lett.* **2019**, *114*, 113502.
- (41) Shah, J. *Ultrafast Spectroscopy of Semiconductors and Semiconductor Nanostructures*; Springer: Berlin, 2013.
- (42) Dal Conte, S.; Bottegoni, F.; Pogna, E.; De Fazio, D.; Ambrogio, S.; Bargigia, I.; D'Andrea, C.; Lombardo, A.; Bruna, M.; Ciccacci, F.; et al. Ultrafast Valley Relaxation Dynamics in Monolayer MoS<sub>2</sub> Probed by Nonequilibrium Optical Techniques. *Phys. Rev. B: Condens. Matter Mater. Phys.* **2015**, *92*, 235425.
- (43) Nie, Z.; Long, R.; Sun, L.; Huang, C.-C.; Zhang, J.; Xiong, Q.; Hewak, D. W.; Shen, Z.; Prezhdo, O. V.; Loh, Z.-H. Ultrafast Carrier Thermalization and Cooling Dynamics in Few-Layer MoS<sub>2</sub>. *ACS Nano* **2014**, *8*, 10931–10940.
- (44) Pogna, E. A.; Marsili, M.; De Fazio, D.; Dal Conte, S.; Manzoni, C.; Sangalli, D.; Yoon, D.; Lombardo, A.; Ferrari, A. C.; Marini, A.; et al. Photo-Induced Bandgap Renormalization Governs the Ultrafast Response of Single-Layer MoS<sub>2</sub>. *ACS Nano* **2016**, *10*, 1182–1188.
- (45) Steinleitner, P.; Merkl, P.; Nagler, P.; Mornhinweg, J.; Schüller, C.; Korn, T.; Chernikov, A.; Huber, R. Direct Observation of Ultrafast Exciton Formation in a Monolayer of WSe<sub>2</sub>. *Nano Lett.* **2017**, *17*, 1455–1460.
- (46) Cui, Q.; Ceballos, F.; Kumar, N.; Zhao, H. Transient Absorption Microscopy of Monolayer and Bulk WSe<sub>2</sub>. *ACS Nano* **2014**, *8*, 2970–2976.
- (47) Sun, D.; Rao, Y.; Reider, G. A.; Chen, G.; You, Y.; Brézin, L.; Harutyunyan, A. R.; Heinz, T. F. Observation of Rapid Exciton-Exciton Annihilation in Monolayer Molybdenum Disulfide. *Nano Lett.* **2014**, *14*, 5625–5629.
- (48) Docherty, C. J.; Parkinson, P.; Joyce, H. J.; Chiu, M.-H.; Chen, C.-H.; Lee, M.-Y.; Li, L.-J.; Herz, L. M.; Johnston, M. B. Ultrafast Transient Terahertz Conductivity of Monolayer MoS<sub>2</sub> and WSe<sub>2</sub> Grown by Chemical Vapor Deposition. *ACS Nano* **2014**, *8*, 11147–11153.
- (49) Ceballos, F.; Zhao, H. Ultrafast Laser Spectroscopy of Two-Dimensional Materials beyond Graphene. *Adv. Funct. Mater.* **2017**, *27*, 1604509.
- (50) Kubo, A.; Onda, K.; Petek, H.; Sun, Z. J.; Jung, Y. S.; Kim, H. K. Femtosecond Imaging of Surface Plasmon Dynamics in a Nanostructured Silver Film. *Nano Lett.* **2005**, *5*, 1123–1127.
- (51) Fukumoto, K.; Yamada, Y.; Onda, K.; Koshihara, S.-Y. Direct Imaging of Electron Recombination and Transport on a Semi-

- conductor Surface by Femtosecond Time-Resolved Photoemission Electron Microscopy. *Appl. Phys. Lett.* **2014**, *104*, 053117.
- (52) Man, M. K. L.; Margiolakis, A.; Deckoff-Jones, S.; Harada, T.; Wong, E. L.; Krishna, M. B. M.; Madeo, J.; Winchester, A.; Lei, S.; Vajtai, R.; Ajayan, P. M.; Dani, K. M. Imaging the Motion of Electrons across Semiconductor Heterojunctions. *Nat. Nanotechnol.* **2017**, *12*, 36–40.
- (53) Doherty, T. A. S.; Winchester, A. J.; Macpherson, S.; Johnstone, D. N.; Pareek, V.; Tennyson, E. M.; Kosar, S.; Kosasih, F. U.; Anaya, M.; Abdi-Jalebi, M.; Andaji-Garmaroudi, Z.; Wong, E. L.; Madéo, J.; Chiang, Y.-H.; Park, J.-S.; Jung, Y.-K.; Petoukhoff, C. E.; Divitini, G.; Man, M. K. L.; Ducati, C.; et al. Performance-Limiting Nanoscale Trap Clusters at Grain Junctions in Halide Perovskites. *Nature* **2020**, *580*, 360–366.
- (54) Wang, L.; Xu, C.; Li, M. Y.; Li, L. J.; Loh, Z.-H. Unraveling Spatially Heterogeneous Ultrafast Carrier Dynamics of Single-Layer WSe<sub>2</sub> by Femtosecond Time-Resolved Photoemission Electron Microscopy. *Nano Lett.* **2018**, *18*, 5172–5178.
- (55) Bauer, E. *Surface Microscopy with Low Energy Electrons*; Springer: New York, 2014.
- (56) Sedghi, G.; Garcia-Suarez, V. M.; Esdaile, L. J.; Anderson, H. L.; Lambert, C. J.; Martin, S.; Bethell, D.; Higgins, S. J.; Elliott, M.; Bennett, N.; Macdonald, J. E.; Nichols, R. J. Long-Range Electron Tunnelling in Oligo-Porphyrin Molecular Wires. *Nat. Nanotechnol.* **2011**, *6*, 517–523.
- (57) Lee, C.; Yan, H.; Brus, L. E.; Heinz, T. F.; Hone, J.; Ryu, S. Anomalous Lattice Vibrations of Single- and Few-Layer MoS<sub>2</sub>. *ACS Nano* **2010**, *4*, 2695–2700.
- (58) Zhang, X.; Han, W. P.; Wu, J. B.; Milana, S.; Lu, Y.; Li, Q. Q.; Ferrari, A. C.; Tan, P. H. Raman Spectroscopy of Shear and Layer Breathing Modes in Multilayer MoS<sub>2</sub>. *Phys. Rev. B: Condens. Matter Mater. Phys.* **2013**, *87*, 115413.
- (59) Mak, K. F.; He, K.; Lee, C.; Lee, G. H.; Hone, J.; Heinz, T. F.; Shan, J. Tightly Bound Trions in Monolayer MoS<sub>2</sub>. *Nat. Mater.* **2013**, *12*, 207–211.
- (60) Bhanu, U.; Islam, M. R.; Tetard, L.; Khondaker, S. I. Photoluminescence Quenching in Gold - MoS<sub>2</sub> Hybrid Nanoflakes. *Sci. Rep.* **2015**, *4*, 5575.
- (61) Turro, N. J. *Modern Molecular Photochemistry*; University Science Books: Sausalito, CA, 1991.
- (62) Prasai, D.; Klots, A. R.; Newaz, A.; Niezgoda, J. S.; Orfield, N. J.; Escobar, C. A.; Wynn, A.; Efimov, A.; Jennings, G. K.; Rosenthal, S. J.; et al. Electrical Control of Near-Field Energy Transfer between Quantum Dots and Two-Dimensional Semiconductors. *Nano Lett.* **2015**, *15*, 4374–4380.
- (63) Buscema, M.; Steele, G. A.; van der Zant, H. S. J.; Castellanos-Gomez, A. The Effect of the Substrate on the Raman and Photoluminescence Emission of Single-Layer MoS<sub>2</sub>. *Nano Res.* **2014**, *7*, 561–571.
- (64) Li, Y.; Qi, Z.; Liu, M.; Wang, Y.; Cheng, X.; Zhang, G.; Sheng, L. Photoluminescence of Monolayer MoS<sub>2</sub> on LaAlO<sub>3</sub> and SrTiO<sub>3</sub> Substrates. *Nanoscale* **2014**, *6*, 15248–15254.
- (65) Yu, Y.; Yu, Y.; Xu, C.; Cai, Y.-Q.; Su, L.; Zhang, Y.; Zhang, Y.-W.; Gundogdu, K.; Cao, L. Engineering Substrate Interactions for High Luminescence Efficiency of Transition-Metal Dichalcogenide Monolayers. *Adv. Funct. Mater.* **2016**, *26*, 4733–4739.
- (66) Liu, D.; Yan, X.-Q.; Guo, H.-W.; Liu, Z.-B.; Zhou, W.-Y.; Tian, J.-G. Substrate Effect on the Photoluminescence of Chemical Vapor Deposition Transferred Monolayer WSe<sub>2</sub>. *J. Appl. Phys.* **2020**, *128*, 043101.
- (67) Nie, Z.; Shi, Y.; Qin, S.; Wang, Y.; Jiang, H.; Zheng, Q.; Cui, Y.; Meng, Y.; Song, F.; Wang, X.; Turcu, I. C. E.; Wang, X.; Xu, Y.; Shi, Y.; Zhao, J.; Zhang, R.; Wang, F. Tailoring Exciton Dynamics of Monolayer Transition Metal Dichalcogenides by Interfacial Electron-Phonon Coupling. *Commun. Phys.* **2019**, *2*, 103.
- (68) Lippert, S.; Schneider, L. M.; Renaud, D.; Kang, K. N.; Ajayi, O.; Kuhnert, J.; Halbich, M.-U.; Abdulmunem, O. M.; Lin, X.; Hassoon, K.; Edalati-Boostan, S.; Kim, Y. D.; Heimbrot, W.; Yang, E.-H.; Hone, J. C.; Rahimi-Iman, A. Influence of the Substrate Material on the Optical Properties of Tungsten Diselenide Monolayers. *2D Mater.* **2017**, *4*, 025045.
- (69) Goodman, A. J.; Lien, D. H.; Ahn, G. H.; Spiegel, L. L.; Amani, M.; Willard, A. P.; Jaye, A.; Tisdale, W. A. Substrate-Dependent Exciton Diffusion and Annihilation in Chemically Treated MoS<sub>2</sub> and WS<sub>2</sub>. *J. Phys. Chem. C* **2020**, *124*, 12175–12184.
- (70) Schneider, C.; Glazov, M. M.; Korn, T.; Höfling, S.; Urbaszek, B. Two-Dimensional Semiconductors in the Regime of Strong Light-Matter Coupling. *Nat. Commun.* **2018**, *9*, 2695.
- (71) Hou, S.; Tobing, L. Y. M.; Wang, X.; Xie, Z.; Yu, J.; Zhou, J.; Zhang, D.; Dang, C.; Coquet, P.; Tay, B. K.; Birowosuto, M. D.; Teo, E. H. T.; Wang, H. Manipulating Coherent Light-Matter Interaction: Continuous Transition between Strong Coupling and Weak Coupling in MoS<sub>2</sub> Monolayer Coupled with Plasmonic Nanocavities. *Adv. Opt. Mater.* **2019**, *7*, 1900857.
- (72) Hüfner, S. *Photoelectron Spectroscopy: Principles and Applications*; Springer: Berlin, 2013.
- (73) Fann, W. S.; Storz, R.; Tom, H. W. K.; Bokor, J. Electron Thermalization in Gold. *Phys. Rev. B: Condens. Matter Mater. Phys.* **1992**, *46*, 13592–13595.
- (74) Yu, Y.; Ji, Z. H.; Zu, S.; Du, B. W.; Kang, Y. M.; Li, Z. W.; Zhou, Z. K.; Shi, K. B.; Fang, Z. Y. Ultrafast Plasmonic Hot Electron Transfer in Au Nanoantenna/MoS<sub>2</sub> Heterostructures. *Adv. Funct. Mater.* **2016**, *26*, 6394–6401.
- (75) Grubisic Cabo, A.; Miwa, J. A.; Grønborg, S. S.; Riley, J. M.; Johannsen, J. C.; Cacho, C.; Alexander, O.; Chapman, R. T.; Springate, E.; Grioni, M.; Lauritsen, J. V.; King, P. D. C.; Hofmann, P.; Ulstrup, S. Observation of Ultrafast Free Carrier Dynamics in Single Layer MoS<sub>2</sub>. *Nano Lett.* **2015**, *15*, 5883–5887.
- (76) Goswami, T.; Rani, R.; Hazra, K. S.; Ghosh, H. N. Ultrafast Carrier Dynamics of the Exciton and Trion in MoS<sub>2</sub> Monolayers Followed by Dissociation Dynamics in Au@MoS<sub>2</sub> 2D Heterointerfaces. *J. Phys. Chem. Lett.* **2019**, *10*, 3057–3063.
- (77) Becker, W. Fluorescence Lifetime Imaging - Techniques and Applications. *J. Microsc.* **2012**, *247*, 119–136.
- (78) Gray, H. B.; Winkler, J. R. Electron Tunneling through Proteins. *Q. Rev. Biophys.* **2003**, *36*, 341–372.
- (79) Oevering, H.; Paddon-Row, M. N.; Heppener, M.; Oliver, A. M.; Cotsaris, E.; Verhoeven, J. W.; Hush, N. S. Long-Range Photoinduced through-Bond Electron Transfer and Radiative Recombination via Rigid Nonconjugated Bridges: Distance and Solvent Dependence. *J. Am. Chem. Soc.* **1987**, *109*, 3258–3269.
- (80) He, J.; Chen, F.; Li, J.; Sankey, O. F.; Terazono, Y.; Herrero, C.; Gust, D.; Moore, T. A.; Moore, A. L.; Lindsay, S. M. Electronic Decay Constant of Carotenoid Polyenes from Single-Molecule Measurements. *J. Am. Chem. Soc.* **2005**, *127*, 1384–1385.
- (81) Wang, C. S.; Batsanov, A. S.; Bryce, M. R.; Martin, S.; Nichols, R. J.; Higgins, S. J.; Garcia-Suarez, V. M.; Lambert, C. J. Oligoyne Single Molecule Wires. *J. Am. Chem. Soc.* **2009**, *131*, 15647–15654.
- (82) Weiss, E. A.; Ahrens, M. J.; Sinks, L. E.; Gusev, A. V.; Ratner, M. A.; Wasielewski, M. R. Making a Molecular Wire: Charge and Spin Transport through Para-Phenylenes Oligomers. *J. Am. Chem. Soc.* **2004**, *126*, 5577–5584.
- (83) Bruix, A.; Miwa, J. A.; Hauptmann, N.; Wegner, D.; Ulstrup, S.; Grønborg, S. S.; Sanders, C. E.; Dendzik, M.; Grubisic Cabo, A.; Bianchi, M.; Lauritsen, J. V.; Khajetoorians, A. A.; Hammer, B.; Hofmann, P. Single-Layer MoS<sub>2</sub> on Au(111): Band Gap Renormalization and Substrate Interaction. *Phys. Rev. B: Condens. Matter Mater. Phys.* **2016**, *93*, 165422.
- (84) Wilson, N. R.; Nguyen, P. V.; Seyler, K.; Rivera, P.; Marsden, A. J.; Laker, Z. P. L.; Constantinescu, G. C.; Kandyba, V.; Barinov, A.; Hine, N. D. M.; Xu, X.; Cobden, D. H. Determination of Band Offsets, Hybridization, and Exciton Binding in 2D Semiconductor Heterostructures. *Sci. Adv.* **2017**, *3*, No. e1601832.
- (85) Kumar, N.; He, J.; He, D.; Wang, Y.; Zhao, H. Charge Carrier Dynamics in Bulk MoS<sub>2</sub> Crystal Studied by Transient Absorption Microscopy. *J. Appl. Phys.* **2013**, *113*, 133702.
- (86) Zhang, Z. S.; Liu, L. H.; Fang, W. H.; Long, R.; Tokina, M. V.; Prezhdo, O. V. Plasmon-Mediated Electron Injection from Au

- Nanorods into MoS<sub>2</sub>: Traditional *versus* Photoexcitation Mechanism. *Chem.* **2018**, *4*, 1112–1127.
- (87) Neukirch, A. J.; Guo, Z. Y.; Prezhdo, O. V. Time-Domain *ab Initio* Study of Phonon-Induced Relaxation of Plasmon Excitations in a Silver Quantum Dot. *J. Phys. Chem. C* **2012**, *116*, 15034–15040.
- (88) Chen, F.; Hihath, J.; Huang, Z. F.; Li, X. L.; Tao, N. J. Measurement of Single-Molecule Conductance. *Annu. Rev. Phys. Chem.* **2007**, *58*, 535–564.
- (89) Aradhya, S. V.; Venkataraman, L. Single-Molecule Junctions beyond Electronic Transport. *Nat. Nanotechnol.* **2013**, *8*, 399–410.
- (90) Davis, W. B.; Svec, W. A.; Ratner, M. A.; Wasielewski, M. R. Molecular-Wire Behaviour in P-Phenylenevinylene Oligomers. *Nature* **1998**, *396*, 60–63.
- (91) Kang, J.; Liu, W.; Sarkar, D.; Jena, D.; Banerjee, K. Computational Study of Metal Contacts to Monolayer Transition-Metal Dichalcogenide Semiconductors. *Phys. Rev. X* **2014**, *4*, 031005.
- (92) Clavero, C. Plasmon-Induced Hot-Electron Generation at Nanoparticle/Metal-Oxide Interfaces for Photovoltaic and Photocatalytic Devices. *Nat. Photonics* **2014**, *8*, 95–103.
- (93) Brongersma, M. L.; Halas, N. J.; Nordlander, P. Plasmon-Induced Hot Carrier Science and Technology. *Nat. Nanotechnol.* **2015**, *10*, 25–34.
- (94) Cadiz, F.; Courtade, E.; Robert, C.; Wang, G.; Shen, Y.; Cai, H.; Taniguchi, T.; Watanabe, K.; Carrere, H.; Lagarde, D.; Manca, M.; Amand, T.; Renucci, P.; Tongay, S.; Marie, X.; Urbaszek, B. Excitonic Linewidth Approaching the Homogeneous Limit in MoS<sub>2</sub>-Based van der Waals Heterostructures. *Phys. Rev. X* **2017**, *7*, 021026.
- (95) Novoselov, K. S.; Jiang, D.; Schedin, F.; Booth, T.; Khotkevich, V.; Morozov, S.; Geim, A. K. Two-Dimensional Atomic Crystals. *Proc. Natl. Acad. Sci. U. S. A.* **2005**, *102*, 10451–10453.
- (96) Taghavi, N. S.; Gant, P.; Huang, P.; Niehues, I.; Schmidt, R.; Michaelis de Vasconcellos, S.; Bratschitsch, R.; García-Hernández, M.; Frisenda, R.; Castellanos-Gómez, A. Thickness Determination of MoS<sub>2</sub>, MoSe<sub>2</sub>, WS<sub>2</sub> and WSe<sub>2</sub> on Transparent Stamps Used for Deterministic Transfer of 2D Materials. *Nano Res.* **2019**, *12*, 1691–1695.
- (97) Ferrari, A. C.; Basko, D. M. Raman Spectroscopy as a Versatile Tool for Studying the Properties of Graphene. *Nat. Nanotechnol.* **2013**, *8*, 235–246.
- (98) Castellanos-Gómez, A.; Buscema, M.; Molenaar, R.; Singh, V.; Janssen, L.; van der Zant, H. S. J.; Steele, G. A. Deterministic Transfer of Two-Dimensional Materials by All-Dry Viscoelastic Stamping. *2D Mater.* **2014**, *1*, 011002.
- (99) Ferrari, A. C.; Meyer, J. C.; Scardaci, V.; Casiraghi, C.; Lazzeri, M.; Mauri, F.; Piscanec, S.; Jiang, D.; Novoselov, K. S.; Roth, S.; Geim, A. K. Raman Spectrum of Graphene and Graphene Layers. *Phys. Rev. Lett.* **2006**, *97*, 187401.
- (100) Shearer, C. J.; Slattery, A. D.; Stapleton, A. J.; Shapter, J. G.; Gibson, C. T. Accurate Thickness Measurement of Graphene. *Nanotechnology* **2016**, *27*, 125704.
- (101) Jain, A.; Bharadwaj, P.; Heeg, S.; Parzefall, M.; Taniguchi, T.; Watanabe, K.; Novotny, L. Minimizing Residues and Strain in 2D Materials Transferred from PDMS. *Nanotechnology* **2018**, *29*, 265203.
- (102) Peña Román, R. J.; Auad, Y.; Grasso, L.; Alvarez, F.; Barcelos, I. D.; Zagonel, L. F. Tunneling-Current-Induced Local Excitonic Luminescence in P-Doped WSe<sub>2</sub> Monolayers. *Nanoscale* **2020**, *12*, 13460–13470.
- (103) Purdie, D. G.; Pugno, N. M.; Taniguchi, T.; Watanabe, K.; Ferrari, A. C.; Lombardo, A. Cleaning Interfaces in Layered Materials Heterostructures. *Nat. Commun.* **2018**, *9*, 5387.
- (104) Lo, S.-Z. A.; Wang, L.; Loh, Z.-H. Pulse Propagation in Hollow-Core Fiber at High-Pressure Regime: Application to Compression of Tens of  $\mu$ J Pulses and Determination of Nonlinear Refractive Index of Xenon at 1.03  $\mu$ m. *Appl. Opt.* **2018**, *57*, 4659–4664.
- (105) Aeschlimann, M.; Brixner, T.; Fischer, A.; Kramer, C.; Melchior, P.; Pfeiffer, W.; Schneider, C.; Strüber, C.; Tuchscherer, P.; Voronine, D. V. Coherent Two-Dimensional Nanoscopy. *Science* **2011**, *333*, 1723–1726.
- (106) Kresse, G.; Furthmüller, J. Efficient Iterative Schemes for *ab Initio* Total-Energy Calculations Using a Plane-Wave Basis Set. *Phys. Rev. B: Condens. Matter Mater. Phys.* **1996**, *54*, 11169–11186.
- (107) Perdew, J. P.; Burke, K.; Ernzerhof, M. Generalized Gradient Approximation Made Simple. *Phys. Rev. Lett.* **1996**, *77*, 3865–3868.
- (108) Blöchl, P. E. Projector Augmented-Wave Method. *Phys. Rev. B: Condens. Matter Mater. Phys.* **1994**, *50*, 17953–17979.
- (109) Grimme, S.; Antony, J.; Ehrlich, S.; Krieg, H. A Consistent and Accurate *ab Initio* Parametrization of Density Functional Dispersion Correction (DFT-D) for the 94 Elements H–Pu. *J. Chem. Phys.* **2010**, *132*, 154104.
- (110) Monkhorst, H. J.; Pack, J. D. Special Points for Brillouin-Zone Integrations. *Phys. Rev. B* **1976**, *13*, 5188–5192.